

# Waveguide-Integrated Two-Dimensional Material Photodetectors in Thin-Film Lithium Niobate

Sha Zhu, Yiwen Zhang, Yi Ren, Yongji Wang, Kunpeng Zhai, Hanke Feng, Ya Jin, Zezhou Lin, Jiaxue Feng, Siyuan Li, Qi Yang, Ning Hua Zhu, Edwin Yue-Bun Pun,\* and Cheng Wang\*


Thin-film lithium niobate on insulator (LNOI) is a promising platform for optical communications, microwave photonics, and quantum technologies. While many high-performance devices like electro-optic modulators and frequency comb sources have been achieved on LNOI platform, it remains challenging to realize photodetectors (PDs) on LNOI platform using simple and low-cost fabrication techniques. 2D materials are excellent candidates to achieve photodetection since they feature strong light-matter interaction, excellent mechanical flexibility, and potential large-scale complementary metal-oxide-semiconductor-compatible fabrication. Herein, this demand is addressed using an LNOI-2D material platform, and two types of high-performance LNOI waveguide-integrated 2D material PDs, namely graphene and tellurium (Te), are addressed. Specifically, the LNOI-graphene PDs feature broadband operations at telecom and visible wavelengths, high normalized photocurrent-to-dark current ratios up to  $3 \times 10^6 \text{ W}^{-1}$ , and large 3-dB photoelectric bandwidths of  $\approx 40 \text{ GHz}$ , simultaneously. The LNOI-Te PDs on the other hand provide ultrahigh responsivities of  $7 \text{ A W}^{-1}$  under  $0.5 \text{ V}$  bias for telecom signals while supporting GHz frequency responses. The results show that the versatile properties of 2D materials and their excellent compatibility with LNOI waveguides could provide important low-cost solutions for system operating point monitoring and high-speed photoelectric conversion in future LNOI photonic integrated circuits.

## 1. Introduction

Photonic integration plays an important role in future ultrahigh-speed optical communications, microwave signal processing, as well as quantum computation and communications. Lithium niobate (LN) is one of the most promising optical materials for future integrated photonics, exhibiting a high electro-optic coefficient ( $r_{33} = 27 \text{ pm V}^{-1}$ ), relatively large refractive indices ( $n_o = 2.21$  and  $n_e = 2.14$ ), a wide transparency window, and low-optic losses.<sup>[1]</sup> Traditional LN devices formed by titanium in-diffusion or proton exchange typically feature weak optical confinement due to the low refractive index contrast ( $\approx 0.02$ ) and as a result compromised device performance. In comparison, the recently emerged thin-film LN platform benefits from a much larger index contrast and has enabled a range of compact and high-performance integrated photonic components, including electro-optic modulators,<sup>[2]</sup> frequency combs,<sup>[3]</sup> delay lines,<sup>[4]</sup> lasers,<sup>[5]</sup> optical filters,<sup>[6]</sup> acousto-optic modulators,<sup>[7]</sup> and so on. More importantly, the commercial availability of high-quality

S. Zhu, J. Feng  
College of Microelectronics  
Faculty of Information Technology  
Beijing University of Technology  
Beijing 100124, China

S. Zhu, Y. Zhang, H. Feng, E. Y. B. Pun, C. Wang  
Department of Electrical Engineering and State Key Laboratory of  
Terahertz and Millimeter Waves  
City University of Hong Kong  
Kowloon, Hong Kong 999077, China  
E-mail: eeeybpun@cityu.edu.hk; cwang257@cityu.edu.hk

 The ORCID identification number(s) for the author(s) of this article can be found under <https://doi.org/10.1002/adpr.202300045>.

© 2023 The Authors. Advanced Photonics Research published by Wiley-VCH GmbH. This is an open access article under the terms of the Creative Commons Attribution License, which permits use, distribution and reproduction in any medium, provided the original work is properly cited.

DOI: 10.1002/adpr.202300045

Y. Ren, Y. Wang, S. Li, Q. Yang  
Department of Chemistry  
City University of Hong Kong  
Hong Kong 999077, China

K. Zhai, Y. Jin, N. H. Zhu  
State Key Laboratory on Integrated Optoelectronics  
Institute of Semiconductors  
Chinese Academy of Sciences  
Beijing 100083, China

Z. Lin  
Department of Applied Physics and Research Institute for Smart Energy  
The Hong Kong Polytechnic University  
Hong Kong 999077, China

lithium niobate on insulator (LNOI) wafers at scales up to 6 inches and the recent demonstration of wafer-scale device manufacturing processes have further boosted the competitiveness of the LNOI platform in terms of scalability, cost-effectiveness, and commercial readiness.<sup>[8]</sup>

Photodetectors (PDs) are indispensable components for recovering transmitted signals in optical communications, photo-electric conversion in microwave photonics, and monitoring system bias points in large-scale photonic networks.<sup>[9]</sup> Nevertheless, integrating PDs on the LNOI platform has remained a substantial challenge due to LN's large bandgap that leads to high transparency (i.e., low absorbance) in both visible and infrared wavelengths, as well as lattice mismatch issues that prevent the epitaxial growth of III-V materials on LN. Attempts have been made to heterogeneously integrate III-V PDs with LNOI devices via die bonding.<sup>[10]</sup> Such processes, however, require expensive and complicated alignment and bonding tools to achieve good yield at large scales. More scalable and cost-effective integration of PDs on the LNOI platform could be realized using deposited amorphous silicon, which however works in the visible wavelength range only.<sup>[11]</sup>

Two-dimensional (2D) materials could become an excellent alternative to achieve PDs on the LNOI platform in a simple and widely compatible way. Stacked via van der Waals forces, the atomically thin layers of 2D materials feature strong light-matter interactions, superior mechanical flexibility, and good chemical stability without surface dangling bonds,<sup>[12]</sup> leading to high responsivities, good long-term operational stability, and excellent compatibility with different photonic materials and structures. In particular, waveguide-integrated 2D-material PDs feature strong light-matter interaction and low carrier transit time, therefore are ideal solutions for photoelectric conversion in planar photonic integrated circuits.<sup>[13]</sup> Previous LNOI-2D material integration has been demonstrated by integrating graphene with etch-less waveguides on flat LN surfaces, where the bound-state-in-the-continuum (BIC) modes only support low-loss propagation for certain waveguide dimensions,<sup>[14]</sup> as well as by integrating etched waveguides with black phosphorus, which is known to have stability issues in air.<sup>[15]</sup>

Here, we demonstrate a general and versatile LNOI-2D material PD platform by integrating two types of 2D materials with monolithically fabricated LNOI devices without strict lattice matching requirements. Specifically, graphene PDs provide broad electrical and optical operation bandwidths, owing to its ultrahigh carrier mobility, broadband optical absorption, and tunable Fermi level,<sup>[13b,16]</sup> whereas tellurium (Te) PDs feature extremely high responsivities due to the carrier avalanche and photogating effect.<sup>[17]</sup> Furthermore, both graphene and Te feature good long-term stability in air and potentially allow wafer-scale integration with the LNOI platform, i.e., by transferring chemical vapor deposited graphene films and thermal evaporation of Te films.<sup>[18]</sup> We first demonstrate a broadband LNOI-graphene PD operating at both telecommunication and visible bands, with a low dark current of 5 nA and a high normalized photocurrent-to-dark current ratio (NPDR) above  $3 \times 10^6 \text{ W}^{-1}$  at 1550 nm. The LNOI-graphene PD features relatively flat photoelectric responses at frequencies up to 40 GHz. We then demonstrate an LNOI-Te PD with an ultrahigh responsivity of  $7 \text{ A W}^{-1}$  under a 0.5 V bias at 1550 nm and a 3 dB bandwidth

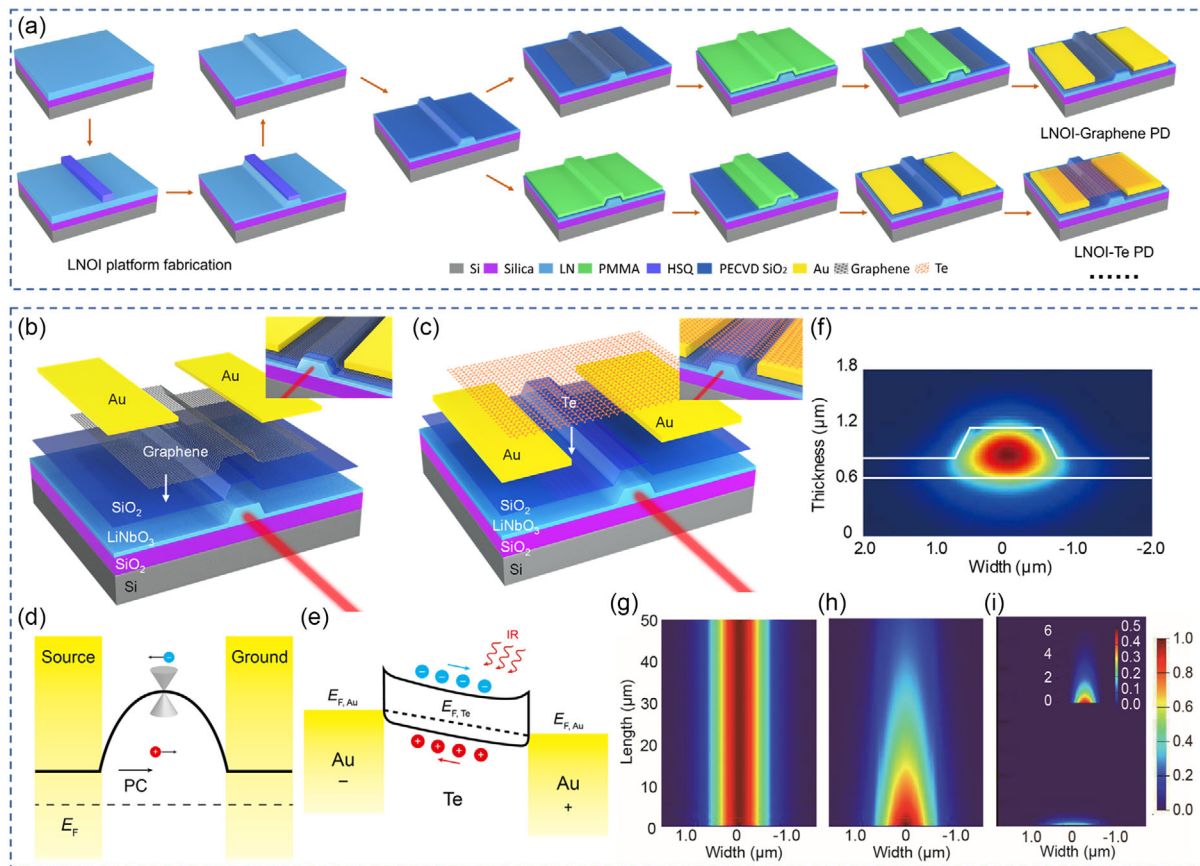
of 2 GHz. The versatile performances provided by our LNOI-2D material platform could serve as important building blocks for various photodetection needs in future LNOI photonic integrated circuits.

Figure 1a–c depicts the fabrication flow and 3D schematics of the two proposed LNOI-2D material PDs. For 2D materials with excellent mechanical flexibility and toughness such as graphene, it can directly cover the surface of LNOI waveguide without any wrinkles and rupture, as shown in Figure 1b. The electrodes are then deposited on top of the transferred graphene. For other 2D materials like Te, we deposit the electrodes first to reduce the height difference between the waveguide and the surrounding plateau, so that the 2D material can be transferred with less stress and potential cracks, as shown in Figure 1c. On the surface of LN, a thin SiO<sub>2</sub> gap layer is deposited for electrical isolation and contamination control.

Figure 1d shows the energy band diagram of the LNOI-graphene PD. Due to the different doping levels between the graphene under gold electrodes (p-doped<sup>[19]</sup>) and the graphene channel (p<sup>+</sup>-doped induced by surrounding air), the interfaces of the two electrodes exhibit obvious band bending, reverse potential gradients, and also a built-in electric field. This enables the operation of our PD in a self-powered state without the need for a DC bias voltage when we design the pair of electrodes to be asymmetric [inset of Figure 1b].<sup>[20]</sup> The potential gradient induced by the gold electrode closer to the waveguide substantially overlaps with the optical field and could efficiently separate the generated photocarriers even at zero bias, while the gold electrode farther from the waveguide moves electrons (or holes) unidirectionally to avoid the cancellation of the overall photocurrent.<sup>[16b,21]</sup> The effective separation of electron-hole pairs in such self-powered PDs thus favors ultrafast response and high responsivity when no external bias is applied.<sup>[22]</sup>

We use finite-difference time-domain (FDTD, Ansys Lumerical) simulation to verify that the optical signal could be efficiently absorbed by our multilayer graphene. In order to be compatible with the waveguide dimensions of commonly reported LNOI photonic devices, especially high-modulation-efficiency LNOI modulators, a 500 nm thick LN film with an etching depth of 250 nm is used in our proposed waveguide-integrated LNOI-2D material PDs. Figure 1f shows the cross-sectional optical eigenmode profile of the LN waveguide for TE<sub>0</sub> mode, which aligns with the largest electro-optic coefficient ( $r_{33}$ ) in our *x*-cut LNOI material and is the most relevant for majority of applications. Figure 1g,h shows the simulated optical transmission performance along the LN waveguide without and with the graphene layer, indicating a strong absorption of optical signals within a few tens of microns. We have also calculated the light absorption for different numbers of graphene layers, as shown in Figure S1, Supporting Information. For single-layer graphene, the absorption coefficient is only  $0.014 \text{ dB } \mu\text{m}^{-1}$ , while for 10-layer graphene used in this work, the absorption coefficient can reach up to  $0.14 \text{ dB } \mu\text{m}^{-1}$ . More detailed simulated electric field intensity evolution for different numbers of layers can be found in Figure S2, Supporting Information.

For the LNOI-Te PD, its energy band diagram under a finite electrical bias is shown in Figure 1e. The short depletion region in Te is drawn mainly due to the good ohmic contact in our devices, which is confirmed in the measured linear IV characteristic



**Figure 1.** a) Fabrication flowchart of the waveguide-integrated 2D material PDs in LNOI platform. 3D schematic and zoom-in view of the b) LNOI-graphene and c) LNOI-Te PDs. Energy band diagrams of the d) LNOI-graphene PD and e) LNOI-Te PDs.  $E_F$ : Fermi level, PC: photocurrent, WG: waveguide, IR: infrared,  $E_{F,Au}$  and  $E_{F,Te}$ : Fermi levels of Au and Te, respectively. f) Simulated optical eigenmode profile (electric field intensity) of the LNOI waveguide. Simulated electric field intensity evolution along the LNOI waveguide g) without 2D material, with 10 layers of h) graphene and i) Te. (Inset in i): zoom-in view of transmission electric field with length on the vertical axis.

in the dark environment to be discussed later. Such ohmic contact originates from a combination of a small Schottky barrier height between Au and Te thanks to the high work function of Au and a small Schottky barrier width and depletion region due to the high hole doping concentration of Te.<sup>[23]</sup> The LNOI-Te PD exhibits a relatively small photocurrent at 0 V bias which will be shown in the following sections, ruling out the possibility that the produced photocurrent is attributed to the photovoltaic effect or the photo-thermoelectric effect. Instead, according to the energy band alignments, the photoconductive effect dominates the produced photocurrent of the LNOI-Te PD.<sup>[17d]</sup> During this process, the photogenerated charge carriers can be produced by absorbing infrared light from the waveguide, and then they are drifted by the electrostatic force and finally collected by gold electrodes. Figure 1h shows the simulated optical transmission performance of the LNOI-Te PD with a large optical absorption of  $3.42 \text{ dB } \mu\text{m}^{-1}$  (Figure S3, Supporting Information). The details of device fabrication and numerical simulation can be found in the Experimental Section.

Next, we perform a detailed material characterization of the fabricated LNOI-2D material devices, which is key to the

performances of the final PDs (Figure 2). For the LNOI-graphene PD, Figure 2a shows its false-colored scanning electron microscope (SEM) image, where the multilayer graphene of about  $56 \mu\text{m}$  in length is tightly attached to the LN waveguide without wrinkles or ruptures, ensuring good conductivity and efficient microscope (AFM) measurement is carried out, which reveals that the thicknesses of multilayer graphene and LN waveguide are about 5 and 250 nm, respectively (Figure 2b). The microscopic atomic structure of the multilayer graphene is further characterized by transmission electron microscopy (TEM), where selected area electron diffraction (SAED) confirms its single crystalline nature (Figure S4, Supporting Information).<sup>[24]</sup> Raman spectra collected at the transferred multilayer graphene area also show clear characteristic Raman peaks at  $1581 \text{ (G)}$  and  $2717 \text{ cm}^{-1} \text{ (2D)}$ ,<sup>[25]</sup> with an intensity ratio of  $2\text{D G}^{-1}$  less than 1, which indicates that the attached material is indeed multilayer graphene (Figure S5, Supporting Information).<sup>[26]</sup> We perform Raman intensity mapping of the PD at  $1581 \text{ cm}^{-1}$  (Figure 2c), confirming that the graphene channel still maintains good integrity and uniformity without cracks and wrinkles after transfer, which lays a solid foundation for the excellent PD performance to be discussed next.

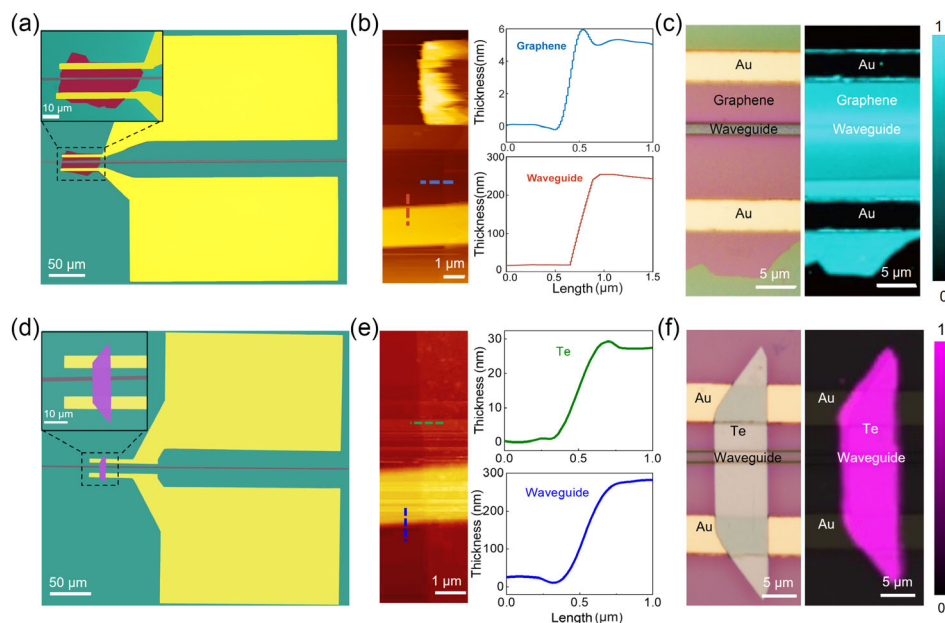


**Figure 2.** a) False-colored scanning electron microscope (SEM) image with zoom-in view, b) atomic force microscope (AFM) image, c) optical image (left) and Raman mapping image (right) of the fabricated LNOI-graphene PD, respectively. d) False-colored SEM image with zoom-in view, e) AFM image, f) optical image (left) and Raman mapping image (right) of the fabricated LNOI-Te PD, respectively.

Similarly, we perform detailed material characterizations of the LNOI-Te PD to confirm its single-crystalline properties and structural integrity after transfer. Figure 2d,f shows the false-colored SEM and Raman intensity mapping of the LNOI-Te PD, confirming the 8  $\mu\text{m}$ -width Te flake covers the LNOI waveguide and electrodes evenly without wrinkles. AFM measurement [Figure 2e] reveals a Te layer height of 27 nm, which provides a bandgap ( $\approx 0.27$  eV) to support light absorption at the telecom band.<sup>[17a,27]</sup> TEM and SAED measurements verify the single crystalline nature of Te (Figure S6, Supporting Information),<sup>[17a]</sup> whereas the Raman peaks [Figure S7, Supporting Information] observed at 92 ( $E_1$ ), 121 ( $A_1$ ), and 140  $\text{cm}^{-1}$  ( $E_2$ , used for Raman mapping in Figure 2f) confirm that the material covering the LN waveguide is indeed Te.<sup>[17a]</sup>

We then show that our LNOI-2D material PDs could provide excellent complementary performances suitable for different application scenarios in future LNOI photonic circuits. In particular, the LNOI-graphene PD provides broadband high-speed photoelectric responses from near-visible to telecom bands with low dark currents. Benefiting from the built-in electric field induced by the asymmetric electrodes, substantial photocurrent ( $I_p$ ) could be generated even at zero bias, allowing for a low dark current ( $I_d$ ) of 5 nA, defined as the current collected at zero input optical power. The measured photocurrent linearly increases with increasing input optical power ( $P_{\text{in}}$ ) without saturation at up to 400  $\mu\text{W}$  on-chip power, as shown in Figure 3a, leading to a measured responsivity of 17.27  $\text{mA W}^{-1}$  at 1550 nm under zero bias. The combination of a good responsivity and low dark current leads to a high normalized photocurrent-to-dark current ratio (NPDR) above  $3 \times 10^6 \text{ W}^{-1}$  [Figure 3a], indicating an excellent signal-to-noise performance in our PDs. Further increasing the length of graphene and coupling the graphene with a

waveguide mode with a stronger evanescent field could lead to higher light absorption and even larger responsivity.<sup>[13a]</sup>

Our LNOI-graphene PD could efficiently operate over a broad wavelength range benefiting from the absence of bandgap in graphene. Figure 3b,c displays the measured responsivity and NPDR under zero bias at different telecom (1500–1630 nm) and near-visible (765–785 nm) wavelengths, showing broadband near-flat spectral responses in both bands. Compared with the telecom band, the responsivity at near-visible is slightly lower ( $\approx 8 \text{ mA W}^{-1}$ ) due to a smaller optical mode and consequently a reduced modal overlap with graphene. Still, it exhibits a high NPDR of  $1.7 \times 10^6 \text{ W}^{-1}$  thanks to the low dark current. Since graphene has no bandgap and our LNOI waveguides support low-loss light transmission over a broad wavelength range, we expect the actual operation bandwidth of our PD to cover the entire visible, near-infrared, and part of the mid-infrared bands (ultimately limited by waveguide cutoff and  $\text{SiO}_2$  material absorption). Furthermore, we show that our LNOI-graphene PD could provide a near-flat frequency response about 40 GHz, as the measured photoelectric  $S_{21}$  in Figure 3d shows. The small increase in  $S_{21}$  at low frequencies could be attributed to an unmatched source impedance in our PD.<sup>[21b]</sup> The photoelectric  $S_{21}$  response of our devices could be flatter by optimizing the electrode parameters and designing the electrode characteristic impedance.<sup>[28]</sup>

The responsivity of the LNOI-graphene PD can be further increased significantly by applying an external DC bias to induce an additional electrical field in the active region (Figure 3e). For positive bias voltages, the responsivity can reach up to 419  $\text{mA W}^{-1}$  at a 1 V bias without observable saturation behavior. The detectivity is  $3.37 \times 10^{11}$  Jones under 1 V bias, which is two orders of magnitude larger than previous reported



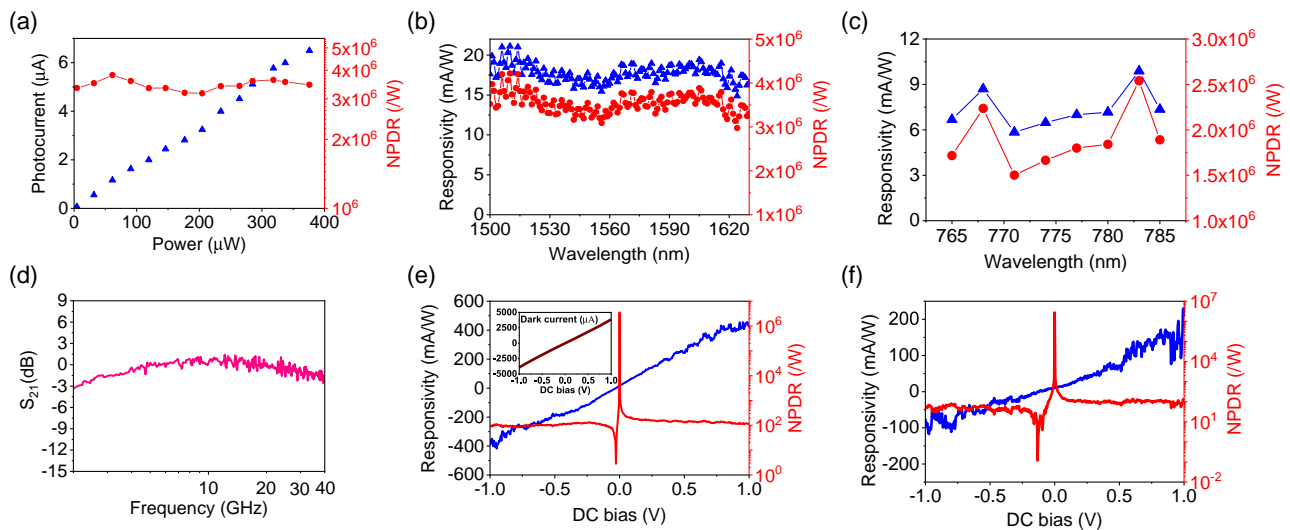


**Figure 3.** a) Measured photocurrent and normalized photocurrent-to-dark-current ratios (NPDR) of the LNOI-graphene PD versus input optical power at 1550 nm under zero bias. Measured responsivity and NPDR at b) telecom and c) visible bands under zero bias. d) Measured photoelectric  $S_{21}$  response at 1550 nm. Measured responsivity and NPDR with respect to DC bias at e) 1550 nm (Inset: dark current versus DC bias) and f) 783 nm wavelength. (The incident light intensities in (b–f) are 60, 35, 60, 49 and 40  $\mu\text{W}$ , respectively).

graphene-photodetector ( $2 \times 10^9$  Jones).<sup>[29]</sup> When the bias voltage turns negative, the internal electrical field is first canceled and then reversed, leading to a negative responsivity. Under  $-0.028$  V DC bias, the responsivity becomes zero. The larger responsivities at finite bias voltages are accompanied with increased dark currents [inset of Figure 3e], leading to lowered NPDR on the order of  $10^2 \text{ W}^{-1}$  [Figure 3e], still comparable with other 2D-material PDs.<sup>[30]</sup> To achieve high responsivity and NPDR simultaneously, LNOI-Te PDs could be used instead, as we discuss next. Similar trend of responsivity increase at finite bias voltages can also be observed in the near-visible band,

reaching  $200 \text{ mA W}^{-1}$  at 1 V and  $-100 \text{ mA W}^{-1}$  at  $-1$  V [Figure 3f]. The small asymmetry between positive and negative bias voltages may be attributed to the differences in the number of impurities at the contact interface between the source-drain metals and semiconductors. Detailed measurement setups and characterization methodologies can be found in the “Experimental Section” and supplementary information.

Finally, we show the LNOI-Te PD could offer ultrahigh responsivity and high NPDR at the same time, ideally suited for system monitoring of photonic circuits. As Figure 4a,b shows, the measured responsivity exceeds  $7 \text{ A W}^{-1}$  at a weak

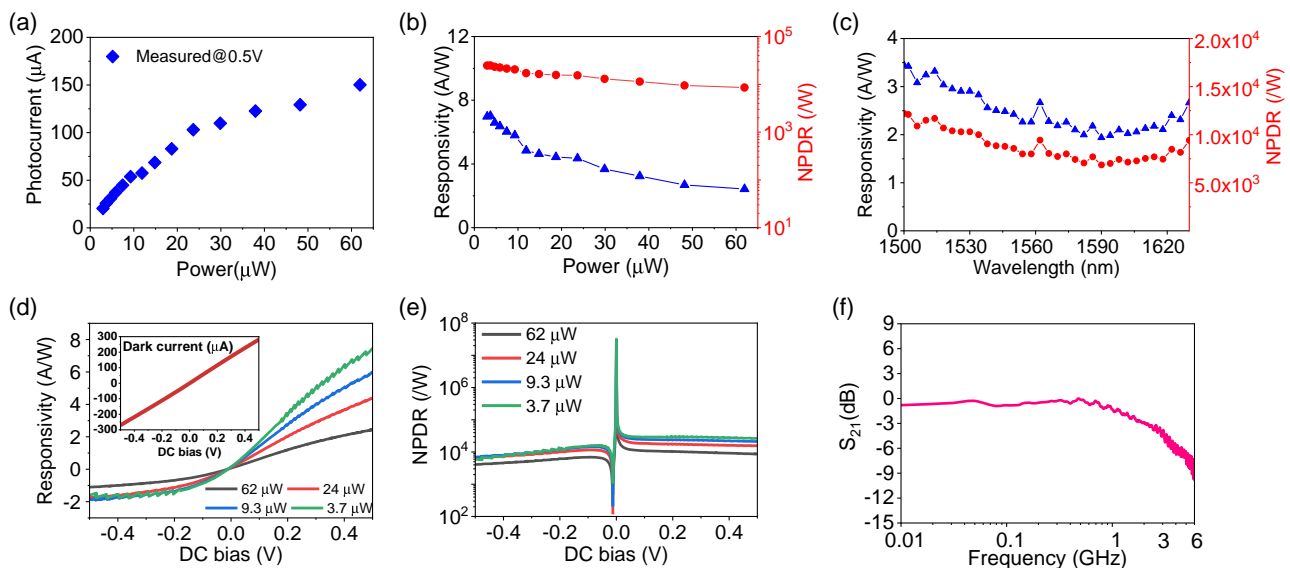


**Figure 4.** a) Measured photocurrent as well as b) responsivity and NPDR versus input optical power at 1550 nm under 0.5 V DC bias. c) Measured responsivity and NPDR from 1500 to 1630 nm wavelength under 0.5 V DC bias. d) Measured responsivity (Inset: dark current versus DC bias) and e) corresponding NPDR versus DC bias at 1550 nm. f) Measured frequency response of the LNOI-Te PD.

input optical power of  $3 \mu\text{W}$  at  $1550 \text{ nm}$  under a bias of  $0.5 \text{ V}$ , thanks to the strong light absorption and high photogain of Te material. The photocurrent sees saturation behavior and reduced responsivities at higher optical powers (but remains  $>2 \text{ A W}^{-1}$  at  $60 \mu\text{W}$ ) due to the limited trap states in Te, as shown in Figure 4a,b. Under zero bias, the LNOI-Te PD shows a small photocurrent and a low responsivity [Figure S8, Supporting Information]. Figure 4c shows the measured responsivity and NPDR from  $1500$  to  $1630 \text{ nm}$  at an optical power of  $50 \mu\text{W}$  under  $0.5 \text{ V}$  bias. The responsivity is nearly flat with high NPDRs on the order of  $10^4 \text{ W}^{-1}$  throughout the measured telecom band. As illustrated in Figure 4d,e, although the dark current does increase with DC bias (inset) similar to that in graphene PD, the LNOI-Te PD benefits from much higher responsivities and lower absolute dark current values, resulting in the high measured NPDRs. The nonlinear responsivity–bias relationship in Figure 4d may be attributed to the limited trap states in 2D Te flakes.<sup>[17d]</sup> Upon increasing source-drain voltage and constant light intensity, the trap states in Te are gradually occupied by charge carriers and ultimately leading to saturation behaviors. We also measure the high-frequency performance of the fabricated LNOI-Te PD, which shows a 3-dB bandwidth of  $2 \text{ GHz}$  [Figure 4f]. The carrier mobility of Te is much smaller than that of graphene, which limits the response speed of the LNOI-Te PD.<sup>[31]</sup> The bandwidths of LNOI-Te PDs could potentially be further increased by using doped materials to realize higher charge mobility and designing narrower channels to reduce the transmit time of photogenerated charge carriers.<sup>[31c,32]</sup> The excellent capability to sense weak optical signals with moderate photoelectric bandwidth make our LNOI-Te PDs ideal for monitoring the variation of optical power in future large-scale LNOI photonic integrated circuits, e.g., DC bias drift of modulators, without the need to tap a substantial power out of the network. **Table 1** shows the performance comparison of black phosphorus, graphene, and Te photodetectors reported previously and in this work. Our LNOI-graphene PD has the highest bandwidth, and LNOI-Te PD shows the largest responsivity.

In summary, we fill the photodetection gap on the LNOI platform by demonstrating two proof-of-concept waveguide-integrated LNOI-2D material PD platforms with complementary performance edges. The broadband LNOI-graphene PDs, with a high NPDR of  $3 \times 10^6 \text{ W}^{-1}$ , a decent responsivity of  $17.27 \text{ mA W}^{-1}$  at zero bias, and a high photoelectric bandwidth about  $40 \text{ GHz}$ , could provide high-speed optical receiving elements in future LNOI-based optical communications and microwave photonic systems. The LNOI-Te PDs with ultrahigh responsivities up to  $7 \text{ A W}^{-1}$  and bandwidths over  $2 \text{ GHz}$  could serve as highly sensitive operating point monitoring components

**Table 1.** Comparison of LNOI-waveguide photodetectors.

Material	Responsivity (bias voltage)	Bandwidth	Reference
Black phosphorus	$2.64 \text{ A W}^{-1}$ ( $2 \text{ V}$ )	$1.97 \text{ GHz}$	[15a]
Black phosphorus	$0.148 \text{ A W}^{-1}$ ( $0.3 \text{ V}$ )	–	[15b]
Graphene	$17.27 \text{ mA W}^{-1}$ ( $0 \text{ V}$ ) $49 \text{ mA W}^{-1}$ ( $0.3 \text{ V}$ )	$\approx 40 \text{ GHz}$	Our work
Te	$7 \text{ A W}^{-1}$ ( $0.5 \text{ V}$ )	$2 \text{ GHz}$	Our work

in future LNOI photonic networks.<sup>[33]</sup> Importantly, our LNOI-2D material platform could potentially be co-fabricated on wafer scales at low cost, by integrating CVD-grown graphene and/or evaporated Te thin films on LNOI wafers processed using stepper lithography processes. Further integrating LNOI waveguides with other 2D materials like transition metal dichalcogenides ( $\text{MoS}_2$ ,  $\text{MoTe}_2$ , and  $\text{WSe}_2$ ) and noble metal dichalcogenides ( $\text{PtSe}_2$  and  $\text{PdSe}_2$ ) may not only provide more versatile photodetection properties but also enable heterojunction or Schottky junction-based PDs with low dark current, high signal-to-noise ratio, small power consumption, as well as large bandwidth.<sup>[29]</sup>

## 2. Experimental Section

**Numerical Simulation:** Ansys Lumerical FDTD software was used to simulate the cross-section eigenmode profiles and electric field intensity evolutions in our LNOI-2D material PDs. A surface conductivity model was used for the multilayer graphene, where a scattering rate of  $15 \text{ meV}$ , a chemical potential of  $0.11 \text{ eV}$ , and a temperature of  $300 \text{ K}$  are employed.<sup>[34]</sup> The complex refractive index of Te was  $n_{\text{Te}} = 4.579 + 0.161i$  at  $1550 \text{ nm}$ . The thicknesses were set according to the AFM measurement results.<sup>[35]</sup> The absorptance was given by  $\eta = 1 - 10^{-0.1\alpha L}$ , where  $L$  is the propagation distance and  $\alpha$  is the mode absorption coefficient in  $\text{dB } \mu\text{m}^{-1}$ .

**Device Fabrication:** The flowchart of the fabrication process of the LNOI-graphene PD is shown in Figure 1a. The LN waveguides were fabricated on a commercial x-cut LNOI wafer (NANOLN) with a  $500 \text{ nm}$ -thick thin-film LN, a  $2 \mu\text{m}$  buried silica layer, and a  $500 \mu\text{m}$  silicon substrate. We defined the optical waveguide using hydrogen silsesquioxane by electron-beam lithography (EBL) and transferred the patterns using an optimized argon plasma-based reactive ion etching process to dry etch a rib LN waveguide with a top width of  $1.2 \mu\text{m}$ , a rib height of  $250 \text{ nm}$ , and a tilted angle of  $45^\circ$ . Then, a  $10 \text{ nm}$   $\text{SiO}_2$  layer was deposited using plasma-enhanced chemical vapor deposition as a protective and insulation layer. Next, for the LNOI-graphene PD, an exfoliated multilayer graphene was transferred to the LN waveguide. An asymmetric electrode pair was defined by EBL and patterned on the LNOI waveguides by thermal evaporation and lift-off. For the LNOI-Te PD, the electrode was first fabricated and then the Te is transferred to cover the LN waveguide and electrodes. The annealing temperatures required for the transfer process and the spin-coated electron-beam resist were  $90$  and  $110^\circ \text{C}$ , respectively. Detail synthesis of Te nanoflakes is shown in supplementary information.

To further improve the scalability of our LNOI-2D material platform in the future, we first fabricated the LNOI photonic devices on a 4-inch wafer scale using our recently developed UV stepper lithography-based process.<sup>[36]</sup> Large-scale manufacturing of graphene and Te was also feasible.

The device structures and the morphologies of the materials were directly observed and recorded by an optical microscope (Nikon LV150N, Japan). SEM images were acquired using Hitachi TM4000. The AFM morphology of the PD was characterized by utilizing a Hitachi AFM 5100 N under air atmosphere. The Raman spectra and mapping profile were obtained from a Reinshaw inVia Raman microscope equipped with a  $532 \text{ nm}$  laser. The diameter of the laser spot was approximately  $1 \mu\text{m}$ . TEM measurement was performed using Philips Tecnai 12 BioTWIN operated at  $120 \text{ kV}$ .

**Device Characterizations:** The DC and high-frequency responses of the PDs were measured based on the setups in Figure S9, Supporting Information. A continuous-wave optical carrier emitted from a laser diode (Santec TSL-550 for telecom, Toptica photonics DL PRO 780S for visible) was sent to a fiber polarization controller to accurately control the polarization state and then coupled into an on-chip LN waveguide. The static responses of the PDs were measured by a precision source/measure unit (Keysight B2902A) at different input optical powers. The input power was calibrated by subtracting the coupling loss between lensed fiber and LNOI chip. Using a spot size converter at the input edge of the LNOI-graphene PD could substantially reduce the coupling loss.<sup>[37]</sup> First, the dark currents

at different DC biases were measured without any optical signal input. Afterward, optical signal was coupled into the PD to measure the photocurrent under various input power intensities, optical wavelengths, and bias voltages. Finally, for the high-frequency response of the PD, the optical signal was modulated by a commercial Mach-Zehnder modulator (EOSPACE 40 + Gb s<sup>-1</sup> modulator) driven by microwave signals from a VNA (E5080B Vector Network Analyzer 100 kHz–53 GHz). The modulated optical signal was then sent to the chip and detected by our PD. The recovered electrical signal was collected by a high-frequency RF probe and sent back to the VNA to obtain the S<sub>21</sub> response.

## Supporting Information

Supporting Information is available from the Wiley Online Library or from the author.

## Acknowledgements

S.Z., Y.Z., Y.R., and Y.W. contributed equally to this work. The authors thank Prof. Jeff Ou for the use of near-visible laser Dr. Wing-Han Wong and Dr. Keelson Shum for their help in device fabrication and measurement. The authors are very thankful for funding from the National Natural Science Foundation of China (61922092); Research Grants Council, University Grants Committee (CityU 11204820, CityU 11212721, N\_CityU113/20); Croucher Foundation (9509005); CityU Strategic Grant 7005458; and the High-end Talent Team Construction Plan of Beijing University of Technology.

## Conflict of Interest

The authors declare no conflict of interest.

## Data Availability Statement

The data that support the findings of this study are available from the corresponding author upon reasonable request.

## Keywords

2D materials, graphene, photodetector, tellurium, thin-film lithium niobate

Received: March 9, 2023

Revised: March 25, 2023

Published online:

- [1] a) D. Zhu, L. Shao, M. Yu, R. Cheng, B. Desiatov, C. J. Xin, Y. Hu, J. Holzgrafe, S. Ghosh, A. Shams-Ansari, E. Puma, N. Sinclair, C. Reimer, M. Zhang, M. Lončar, *Adv. Opt. Photonics* **2021**, *13*, 242; b) D. Sun, Y. Zhang, D. Wang, W. Song, X. Liu, J. Pang, D. Geng, Y. Sang, H. Liu, *Light Sci. Appl.* **2020**, *9*, 197.
- [2] a) M. Xu, M. He, H. Zhang, J. Jian, Y. Pan, X. Liu, L. Chen, X. Meng, H. Chen, Z. Li, X. Xiao, S. Yu, S. Yu, X. Cai, *Nat. Commun.* **2020**, *11*, 3911; b) P. Kharel, C. Reimer, K. Luke, L. He, M. Zhang, *Optica* **2021**, *8*, 357; c) C. Wang, M. Zhang, X. Chen, M. Bertrand, A. Shams-Ansari, S. Chandrasekhar, P. Winzer, M. Lončar, *Nature* **2018**, *562*, 101; d) M. Li, J. Ling, Y. He, U. A. Javid, S. Xue, Q. Lin, *Nat. Commun.* **2020**, *11*, 4123; e) M. He, M. Xu, Y. Ren, J. Jian, Z. Ruan, Y. Xu, S. Gao, S. Sun, X. Wen, L. Zhou, L. Liu, C. Guo, H. Chen, S. Yu, L. Liu, X. Cai, *Nat. Photonics* **2019**, *13*, 359.
- [3] a) M. Zhang, B. Buscaino, C. Wang, A. Shams-Ansari, C. Reimer, R. Zhu, J. M. Kahn, M. Lončar, *Nature* **2019**, *568*, 373; b) C. Wang, M. Zhang, M. Yu, R. Zhu, H. Hu, M. Loncar, *Nat. Commun.* **2019**, *10*, 978; c) M. Yu, Y. Okawachi, R. Cheng, C. Wang, M. Zhang, A. L. Gaeta, M. Lončar, *Light Sci. Appl.* **2020**, *9*, 9.
- [4] J.-X. Zhou, R.-H. Gao, J. Lin, M. Wang, W. Chu, W.-B. Li, D.-F. Yin, L. Deng, Z.-W. Fang, J.-H. Zhang, R.-B. Wu, Y. Cheng, *Chin. Phys. Lett.* **2020**, *37*, 084201.
- [5] a) C. Op de Beek, F. M. Mayor, S. Cuyvers, S. Poelman, J. F. Herrmann, O. Atalar, T. P. McKenna, B. Haq, W. Jiang, J. D. Witmer, G. Roelkens, A. H. Safavi-Naeini, R. Van Laer, B. Kuyken, *Optica* **2021**, *8*, 1288; b) A. Shams-Ansari, D. Renaud, R. Cheng, L. Shao, L. He, D. Zhu, M. Yu, H. R. Grant, L. Johansson, M. Zhang, M. Lončar, *Optica* **2022**, *9*, 408; c) T. Li, K. Wu, M. Cai, Z. Xiao, H. Zhang, C. Li, J. Xiang, Y. Huang, J. Chen, *APL Photonics* **2021**, *6*, 101301.
- [6] A. Prencipe, M. A. Baghban, K. Gallo, *ACS Photonics* **2021**, *8*, 2923.
- [7] L. Wan, Z. Yang, W. Zhou, M. Wen, T. Feng, S. Zeng, D. Liu, H. Li, J. Pan, N. Zhu, W. Liu, Z. Li, *Light Sci. Appl.* **2022**, *11*, 145.
- [8] a) K. Luke, P. Kharel, C. Reimer, L. He, M. Loncar, M. Zhang, *Opt. Express* **2020**, *28*, 24452; b) K. Zhang, W. Sun, Y. Chen, H. Feng, Y. Zhang, Z. Chen, C. Wang *Commun. Phys.* **2023**, *6*, 17.
- [9] a) H. Shu, L. Chang, Y. Tao, B. Shen, W. Xie, M. Jin, A. Netherton, Z. Tao, X. Zhang, R. Chen, B. Bai, J. Qin, S. Yu, X. Wang, J. E. Bowers, *Nature* **2022**, *605*, 457; b) J. Michel, J. Liu, L. C. Kimerling, *Nat. Photonics* **2010**, *4*, 527; c) C. Liu, J. Guo, L. Yu, J. Li, M. Zhang, H. Li, Y. Shi, D. Dai, *Light Sci. Appl.* **2021**, *10*, 123.
- [10] X. Zhang, X. Liu, R. Ma, Z. Chen, Z. Yang, Y. Han, B. Wang, S. Yu, R. Wang, X. Cai, *Opt. Lett.* **2022**, *47*, 4564.
- [11] B. Desiatov, M. Lončar, *Appl. Phys. Lett.* **2019**, *115*, 121108.
- [12] F. Xia, H. Wang, D. Xiao, M. Dubey, A. Ramasubramaniam, *Nat. Photonics* **2014**, *8*, 899.
- [13] a) X. T. Gan, R. J. Shiue, Y. D. Gao, I. Meric, T. F. Heinz, K. Shepard, J. Hone, S. Assefa, D. Englund, *Nat. Photonics* **2013**, *7*, 883; b) X. Wang, Z. Cheng, K. Xu, H. K. Tsang, J.-B. Xu, *Nat. Photonics* **2013**, *7*, 888.
- [14] Z. J. Yu, Y. Wang, B. L. Sun, Y. Y. Tong, J. B. Xu, H. K. Tsang, X. K. Sun, *Adv. Opt. Mater.* **2019**, *7*, 1901306.
- [15] a) Y. Xue, X. Wu, K. Chen, J. Wang, L. Liu, *Opt. Mater. Express* **2023**, *13*, 272; b) S. Wang, R. J. Chapman, B. C. Johnson, I. Krasnokutskaya, J.-L. J. Tambaço, K. Messalea, A. Peruzzo, J. Bullock, *Adv. Opt. Mater.* **2023**, *11*, 2201688; c) Y. Wang, Z. J. Yu, Z. Y. Zhang, B. L. Sun, Y. Y. Tong, J. B. Xu, X. K. Sun, H. K. Tsang, *ACS Photonics* **2020**, *7*, 2643.
- [16] a) C.-H. Liu, Y.-C. Chang, T. B. Norris, Z. Zhong, *Nat. Nanotechnol.* **2014**, *9*, 273; b) X. Gan, R.-J. Shiue, Y. Gao, I. Meric, T. F. Heinz, K. Shepard, J. Hone, S. Assefa, D. Englund, *Nat. Photonics* **2013**, *7*, 883.
- [17] a) M. Amani, C. Tan, G. Zhang, C. Zhao, J. Bullock, X. Song, H. Kim, V. R. Shrestha, Y. Gao, K. B. Crozier, M. Scott, A. Javey, *ACS Nano* **2018**, *12*, 7253; b) Y. Wang, G. Qiu, R. Wang, S. Huang, Q. Wang, Y. Liu, Y. Du, W. A. Goddard, M. J. Kim, X. Xu, P. D. Ye, W. Wu, *Nat. Electron.* **2018**, *1*, 228; c) L. Tong, X. Huang, P. Wang, L. Ye, M. Peng, L. An, Q. Sun, Y. Zhang, G. Yang, Z. Li, F. Zhong, F. Wang, Y. Wang, M. Motlag, W. Wu, G. J. Cheng, W. Hu, *Nat. Commun.* **2020**, *11*, 2308; d) C. Shen, Y. Liu, J. Wu, C. Xu, D. Cui, Z. Li, Q. Liu, Y. Li, Y. Wang, X. Cao, H. Kumazoe, F. Shimojo, A. Krishnamoorthy, R. K. Kalia, A. Nakano, P. D. Vashishta, M. R. Amer, A. N. Abbas, H. Wang, W. Wu, C. Zhou, *ACS Nano* **2020**, *14*, 303.
- [18] a) C. Zhao, C. Tan, D.-H. Lien, X. Song, M. Amani, M. Hettick, H. Y. Y. Nyein, Z. Yuan, L. Li, M. C. Scott, A. Javey, *Nat.*

- Nanotechnol.* **2020**, *15*, 53; b) K. Chang, Z. Li, Y. Gu, K. Liu, K. Chen, *Nano Res.* **2022**, *15*, 9704.
- [19] E. J. H. Lee, K. Balasubramanian, R. T. Weitz, M. Burghard, K. Kern, *Nat. Nanotechnol.* **2008**, *3*, 486.
- [20] F. Xia, T. Mueller, R. Golizadeh-Mojarad, M. Freitag, Y.-M. Lin, J. Tsang, V. Perebeinos, P. Avouris, *Nano Lett.* **2009**, *9*, 1039.
- [21] a) T. Mueller, F. Xia, P. Avouris, *Nat. Photonics* **2010**, *4*, 297; b) F. Xia, T. Mueller, Y.-M. Lin, A. Valdes-Garcia, P. Avouris, *Nat. Nanotechnol.* **2009**, *4*, 839.
- [22] R. Pant, D. K. Singh, A. M. Chowdhury, B. Roul, K. K. Nanda, S. B. Krupanidhi, *Apl Mater.* **2020**, *8*, 020907.
- [23] a) G. Qiu, S. Y. Huang, M. Segovia, P. K. Venuthurumilli, Y. X. Wang, W. Z. Wu, X. F. Xu, P. D. D. Ye, *Nano Lett.* **2019**, *19*, 1955; b) H. Ma, J. H. Wu, Y. P. Wang, C. Y. Zhong, Y. T. Ye, M. L. Wei, R. Yu, Y. Q. Du, B. Tang, C. Sun, Y. L. Shi, C. L. Sun, L. C. Wang, H. M. Zhu, S. Qiao, L. Li, H. T. Lin, *Adv. Opt. Mater.* **2022**, *10*, 2201443.
- [24] J. Li, H. Ji, X. Zhang, X. Wang, Z. Jin, D. Wang, L.-J. Wan, *Chem. Commun.* **2014**, *50*, 11012.
- [25] a) D. Graf, F. Molitor, K. Ensslin, C. Stampfer, A. Jungen, C. Hierold, L. Wirtz, *Nano Lett.* **2007**, *7*, 238; b) H.-L. Tang, M.-H. Chiu, C.-C. Tseng, S.-H. Yang, K.-J. Hou, S.-Y. Wei, J.-K. Huang, Y.-F. Lin, C.-H. Lien, L.-J. Li, *ACS Nano* **2017**, *11*, 12817.
- [26] a) A. C. Ferrari, J. C. Meyer, V. Scardaci, C. Casiraghi, M. Lazzeri, F. Mauri, S. Piscanec, D. Jiang, K. S. Novoselov, S. Roth, A. K. Geim, *Phys. Rev. Lett.* **2006**, *97*, 187401; b) J.-B. Wu, M.-L. Lin, X. Cong, H.-N. Liu, P.-H. Tan, *Chem. Soc. Rev.* **2018**, *47*, 1822.
- [27] a) M. MehediHasan, M. Bhuiyan, M. Azad, S. M. Hasan, *J. Appl. Sci. Technol.* **2006**, *4*, 39; b) D. K. Sang, B. Wen, S. Gao, Y. Zeng, F. Meng, Z. Guo, H. Zhang, *Nanomaterials* **2019**, *9*, 1075; c) J. Qiao, Y. Pan, F. Yang, C. Wang, Y. Chai, W. Ji, *Sci. Bull.* **2018**, *63*, 159.
- [28] Y. W. Zhang, L. B. Shao, J. W. Yang, Z. X. Chen, K. Zhang, K. M. Shum, D. Zhu, C. H. Chan, M. Loncar, C. Wang, *Photonics Res.* **2022**, *10*, 2380.
- [29] C. Liu, J. Guo, L. Yu, J. Li, M. Zhang, H. Li, Y. Shi, D. Dai, *Light Sci. Appl.* **2021**, *10*, 123.
- [30] a) R. Tian, X. Gan, C. Li, X. Chen, S. Hu, L. Gu, D. Van Thourhout, A. Castellanos-Gomez, Z. Sun, J. Zhao, *Light Sci. Appl.* **2022**, *11*, 101; b) P. Ma, Y. Salamin, B. Baeuerle, A. Josten, W. Heni, A. Emboras, J. Leuthold, *ACS Photonics* **2019**, *6*, 154; c) J. Guo, J. Li, C. Liu, Y. Yin, W. Wang, Z. Ni, Z. Fu, H. Yu, Y. Xu, Y. Shi, Y. Ma, S. Gao, L. Tong, D. Dai, *Light Sci. Appl.* **2020**, *9*, 29.
- [31] a) S. H. Mir, V. K. Yadav, J. K. Singh, *ACS Omega* **2020**, *5*, 14203; b) M. Amani, C. L. Tan, G. Zhang, C. S. Zhao, J. Bullock, X. H. Song, H. Kim, V. R. Shrestha, Y. Gao, K. B. Crozier, M. Scott, A. Javey, *Acs Nano* **2018**, *12*, 7253; c) N. Flory, P. Ma, Y. Salamin, A. Emboras, T. Taniguchi, K. Watanabe, J. Leuthold, L. Novotny, *Nat. Nanotechnol.* **2020**, *15*, 118.
- [32] P. V. K. Yadav, B. Ajitha, C. M. A. Ahmed, Y. A. K. Reddy, V. R. M. Reddy, *J. Phys. Chem. Solids* **2022**, *160*, 110350.
- [33] a) S. Xu, J. Wang, S. Yi, W. Zou, *Nat. Commun.* **2022**, *13*, 7970; b) B. Bai, Q. Yang, H. Shu, L. Chang, F. Yang, B. Shen, Z. Tao, J. Wang, S. Xu, W. Xie, W. Zou, W. Hu, J. E. Bowers, X. Wang, *Nat. Commun.* **2023**, *14*, 66.
- [34] L. A. Falkovsky, *J. Phys. Conf. Ser.* **2008**, *129*, 012004.
- [35] A. Ciesielski, L. Skowronski, W. Pacuski, T. Szoplík, *Mater. Sci. Semicond. Process.* **2018**, *81*, 64.
- [36] K. Luke, P. Kharel, C. Reimer, L. Y. He, M. Loncar, M. Zhang, *Opt. Express* **2020**, *28*, 24452.
- [37] C. Hu, A. Pan, T. Li, X. Wang, Y. Liu, S. Tao, C. Zeng, J. Xia, *Opt. Express* **2021**, *29*, 5397.